Validation of a Ray Tracing based guided Lamb wave propagation methodology in aerostructures

SHM Journal
XX(X):1–13

DOI: 10.1177/ToBeAssigned
www.sagepub.com/
SAGE

Fernando Sánchez Iglesias[1], Andrés García Serrano[1], Andrés Pedraza Rodriguez[1] and Antonio Fernández López[1]

Abstract

Accurate modelling of guided Lamb wave propagation is crucial for SHM systems, where a large amount of information and cases are needed to cover all in-service conditions of a structure. Historically finite element methods have proven to be accurate and robust enough to simulate the problem, however they typically require substantial computational resources and each simulation may take a significant amount of time to accomplish. This article presents a comprehensive validation study of a wave propagation methodology based in ray tracing applied to predict the acoustic behavior of lightweight structures. Focused on representative composite materials, particularly carbon fiber-reinforced composites, the study addresses the growing need for accurate and fast simulation tools in industries where lightweight and high-strength materials play a pivotal role, such as aerospace and automotive engineering.

The study presents an examination of the ray tracing method's effectiveness via a combination of experimental coupon tests, ranging from a simple rectangular metallic plate to a representative CFRP structure from the wing lower cover of the UPM-LIBIS UAV. The investigation spans a distribution of possible damage locations, ensuring a comprehensive evaluation of the method's applicability.

Results demonstrate the method's efficacy in predicting the elastic wave propagation characteristics, including transmission, reflection, and absorption within composite structures; and it also its behavior when simulating representative in-service damages, generated both via added masses and real impact damages performed on the test specimen. The validation process involves an in-detail comparison with experimental measurements, evaluating the reliability and applicability of the ray tracing approach.

This research not only contributes to the advancement of predictive modeling for acoustic behavior in composite structures but also addresses the broader implications for industries relying on accurate simulations for design optimization and performance evaluation. The validated ray tracing method has proven to be a valuable tool for engineers and researchers seeking precise predictions of wave propagation in composite materials and its computation speed makes the methodology ideal to contribute to a training database for a future SHM system based in Artificial intelligence.

Keywords

SHM, Ray tracing, Composites, Guided waves

Introduction

Carbon Fiber Reinforced Plastic (CFRP) structures are widely used in various industries: aerospace, automotive, sports equipment, and civil engineering, due to their high strength-to-weight ratio and other desirable mechanical properties. Thanks to improvements in the structural analysis discipline, an engineer can ensure that they meet their respective safety, performance, and durability requirements in their intended applications; crucial for industries such as aerospace where lightweight, high-strength materials are essential for achieving optimal performance and efficiency.

However, even when they present all of these significant advantages, carbon fiber structures may require some special attention as, unlike metallic structures, they are subjected to a much wider range of failure modes, such as: delaminations, fiber breakage, matrix cracking, and impact-induced damage [1–4], some of which may be difficult to asses by visual inspection. Therefore, new and affordable systems must be developed to be able to study the performance of these structures in service.

In this framework is where Structural Health Monitoring (SHM) performs a crucial function, employing various sensing technologies, data acquisition systems and signal processing techniques to be able to monitor the structure periodically or in real time. There are two primary approaches in the field of SHM: data-driven and model-driven [5]. Data-driven methods hinge on structural data to deduce the normal operational state of a structure through machine learning processes. On the other hand, model-driven methods leverage physics-based models to ascertain

[1]Technical University of Madrid, Spain

Corresponding author:
Fernando Sánchez Iglesias, Technical University of Madrid, ETSI Aeronáutica y del Espacio, Plaza Cardenal Cisneros S/N, 28008, Madrid, Spain
Email: f.sanchez.iglesias@upm.es

the health condition of a structure by comparing the models' predictions with the actual structural data[6].

The extraction of damage-sensitive features from the structure and the analysis of these features can be used to detect, quantify and determine the location of damage and, additionally, the system could be used to capture real-time events and assess them[7], or be able to consider even the effect of corrosion[8] and other environmental factors[9].

To achieve this, both methodologies must be fed with data from a sensor network permanently installed in the structure. There are many kinds of sensors currently available in the industry and in this article we focus on ultrasonic inspections, which have historically proven to be a reliable and cheap way of evaluating manufacturing defects or in-service damages. This technique is ideal for lightweight structures, as elastic waves are able to travel large distances with very low attenuation and are very sensitive to typical damages of interest[10].

A significantly complex structure could, therefore, be inspected with a very small number of sensors[11,12]; employing elastic waves with a distributed piezoelectric actuator/sensor network based on the pitch-catch method has proven to be very successful for impact damage detection[13,14] and even for other non typical damages such as crack and corrosion localization[15]. These SHM systems could present many cost advantages when compared with the traditional inspection methods, and could also be used to improve the life prediction of the structure based on its usage[12,16].

Beeing able to extract relevant damage identification parameters and accomplish the objective of these systems still requires a significant effort, in terms of signal analysis and interpretation[17,18] and must be substantiated by relevant testing experience. However, due to the high cost of physical tests, numerical simulation can be especially helpful to predict the elastic wave propagation and may help improve the accuracy of these systems[19]. These data-driven methods, also referred as physics-informed machine learning systems are an emerging methodology that can also significantly aid in the interpretation of SHM data. The basic idea consists on combining physics-based models with data-driven ones taking advantage of both to improve predictive capability in an SHM setting[20].

Numerical simulations provide a very effective way to capture and understand the structural behavior in terms of elastic wave response; general purpose computational codes such as time domain spectral finite element methods[21,22] or explicit finite element methods[19,23–25] are commonly used to calculate the wave propagation, and has proven to be a useful tool when used for training of a physiscs-informed machine learning model[26].

However, finite element or finite difference methods, could present a series of significant disadvantages. Some of the most limiting ones could be:

- Computational Complexity: the methodologies tend to be computationally intensive, especially for large and complex structures. Long computation times and high memory requirements may limit their efficiency, and are usually not suitable for real-time or iterative analyses.
- Grid or Element Discretization: Discretizing the structure into grids or elements may result in some loss of accuracy, difficulties in capturing fine details or aliasing effects on high frequencies. The choice of grid or element size can impact the accuracy and computational cost of the analysis and is usually a limiting factor for the maximum scale of structures to be analyzed.
- Material damping of boundary damping: specifically for the explicit finite element method, introducing damping elements, either as dashpots or material damping, significantly reduces the stable time increment, making it exponentially more costly to solve problems where this effect is relevant on the solution.

For these reasons, and also to increase the reliability of the simulations, there have been multiple attempts of solving the problem without resorting to finite elements in the literature, either analytically[27–29] or using statistics or artificial intelligence[30,31]; some of these methods are able to achieve very good results, but the algorithms studied tend to be too complex to generalize or limited in applicability.

There are, however, other numerical approaches that may breach the problems issued above, specifically, this article focuses on the Ray Tracing Method; which is based on the assumption that the particle motion can be modeled as a number of idealized narrow beams (rays) advanced through the medium by discrete amounts. Tracing the paths of individual rays provides valuable information about wave behavior, including wavefront curvature, mode conversion, reflection, and transmission as the rays interact with the objects present along their path. Ray tracing methods have been extensively developed recently for graphics rendering due to the recent technological developments of high-end graphics cards[32], but have also been continually used historically for science and research in different fields such as astronomy[33] or optical design[34].

Ray tracing, however, is not limited to visual rendering, as it can also be applied to simulate sound propagation in various environments. In the context of acoustics and sound engineering, it involves tracing the paths of sound waves as they interact with the boundaries given by the structure. This technique allows for the modeling of how sound behaves in complex 2D or 3D environments, considering factors such as reflection, diffraction, and absorption

The ray tracing-based approach offers significant advantages over traditional numerical methods in terms of computational efficiency and ease of implementation as it is not limited by an element size, although a large number of rays may be limiting in some applications. It provides a practical tool to analyze wave propagation phenomena and has been widely used in scientific research for many different applications, most notably: ocean acoustics[35,36] or heat transfer[37]. Specifically it has also been previously used in SHM to solve the guided wave propagation problem[38–41] and it has proven its effectiveness.

The solution presented in this article also applies the ray tracing method to solve the general guided elastic wave propagation problem for an arbitrary 2D structure and it aims to provide additional versatility such as accounting for multiple sensors or actuators and adjustable boundary

parameters in order to accurately match experimental data; with the objective of developing an efficient and accurate numerical model that may be later used as part of a complete SHM framework, whether it is to train an artificial intelligence model or to determine relevant damage indicators.

Additionally, the sensor model developed considers a finite area instead of a single spatial point. This is done by many different reasons, but mainly provides a significant advantage when compared with other ray tracing methodologies for the following:

- There is no need to calculate additional eigen-rays to capture the signal at the sensors[35]. The initial ray propagation is already sufficient.
- In cases where the signal wavelength is comparable to the sensor dimensions, the secondary dispersive effect is already taken into account on the recovered signal, and therefore no additional computation is needed.

The main limitation of this approach is that a sufficiently large number of rays must be used to completely capture all possible relevant propagation paths that may reach the sensor, analogous to the number of elements of a finite element model, although its computation is still far more efficient.

The set of test cases presented in this article are focused on validating the ray tracing model and demonstrate its applicability to simulate intact structures and detect possible presence of anomalies.

The validation is performed on the following cases:

- A metallic rectangular aluminium plate is used as an initial validation for an isotropic material. This validation is also used to adjust the boundary reflection parameters of the simulation.
- The simulation is then validated against a representative composite structure, corresponding to the lower wing cover of the LIBIS UAV. Artificial damages are introduced in the structure an dcompared with the simulation results.
- Finally the simulation is validated with a real damage present in the structure. An impact of 7 J generating of a possible representative Barely Visible Impact Damage (BVID) is performed in the LIBIS composite wing. The damage is inspected with tradicional NDT techniques and with the installed PZT sensor network and compared with the simulation results. This is shown in a qualitative way via the Hilbert transform.

Materials and methods

The basic idea behind ray tracing involves tracing the path of straight ideal rays as they travel through the structure. This process simulates the behavior of these ultrasonic waves considering factors like reflection, refraction, dispersion and, indirectly shading. The main steps involved in the analysis are as follows:

- Ray Generation: Rays are cast from the source into the structure. Each ray represents a potential path that the elastic waves could propagate to.
- Intersection Testing: The rays are traced through the structure to determine if and where they intersect with objects in the virtual environment.
- Reflection and Refraction: In case of an intersection reflection and refraction of the rays must be accounted for. Reflected rays are traced in the opposite direction from the surface normal, simulating reflective surfaces. Refracted rays resemble the bending of light as it passes through transparent materials.

  The refracted ray path along the structure is governed with the Snell's law, and at the boundary of two mediums 1 and 2 is expressed as:

$$\frac{\cos\theta_1}{\cos\theta_2} = \frac{v_{p1}}{v_{p2}} \tag{1}$$

  where θ_i and v_{pi} are the incidence angle and phase velocity of the medium i.

  When a ray encounters a boundary a component of the ray energy is reflected and another part is refracted or transmitted. For the particular case in which the ray would reach a segment end (ie. a corner) the ray is eliminated from the model. This approach is taken as a simplification to reduce computational effort, as the effect is negligible for a sufficiently large number of rays and can be minimized considering initial rays that wont intersect any corners of the model on their first propagation step, for example: by choosing an odd number of initial rays.

  The model takes into account the mode conversion phenomena[42,43] at each boundary and therefore, the transmitted and reflected component energy is divided between the different propagation modes.

  The energy of the incident ray E_{iray} is divided between the potentially four rays originating at the intersection point (reflected, transmitted and their respective mode changes) and a remnant energy ε_E that could be lost at the boundary, as follows:

$$E_{iray} = f_1 E_{S0_r} + f_2 E_{A0_r} + f_3 E_{S0_t} + f_4 E_{A0_t} + \varepsilon_E \tag{2}$$

  where E_{S0_r} and E_{A0_r} represent the energy of the symmetric and anti-symmetric reflected rays, E_{S0_t} and E_{A0_t} represent the energy of the symmetric and anti-symmetric transmitted rays and the factors f_i represent the wave energy that is distributed between each of the propagation modes, and they are defined in terms of the fraction of energy transmitted through the boundary f_{tr} and the fraction of energy invested in the mode change f_{mc} as follows, assuming an $S0$ incident ray:

$$\begin{aligned} f_1 &= (1-f_{tr})(1-f_{mc}) \\ f_2 &= (1-f_{tr})f_{mc} \\ f_3 &= f_{tr}(1-f_{mc}) \\ f_4 &= f_{tr}f_{mc} \end{aligned} \tag{3}$$

  considering $f_{tr} < 1$ and $f_{mc} < 1$. Both the factors f_i and the dissipated energy ε_E must be adjusted based on the kind of boundary encountered.

- Recursive Tracing: To simulate complex interactions, the tracing algorithm must involve recursive tracing. In this context, as explained previously, a reflected ray might generate additional rays to simulate secondary reflections, and these rays are then traced recursively also capturing their possible interceptions and newer rays that may be generated.

Wave speed and dispersion in metals

Wave propagation in isotropic plates, such as metals, can be understood by the characteristic Lamb wave equations; initially established by Horace Lamb in 1917 and further developed by Raymond Mindlin in 1951[44]. They define group and phase velocity for waves propagating in an infinite plate, describing two modes of propagation: symmetric ($S0$) and anti-symmetric ($A0$). The Lamb wave equations give a very good approximation of the elastic wave propagation speeds in thin plate objects, however, as the infinite plate is nowhere to be found in reality, the term guided Lamb waves is more commonly used to refer to this real phenomena, as its refers to Lamb-like waves that are guided by the finite dimensions of real objects.

These equations were derived by setting up formalism for a solid plate having infinite extent in the x- and y- directions, and thickness h in the z-direction. Assuming sinusoidal solutions of the wave equation and imposing plane stress conditions at the top and bottom surfaces of the plate a pair of characteristic equations can be found. These are:

$$\begin{aligned} \text{Symmetric}: \frac{\tan qh}{\tan ph} &= -\frac{4k^2qp}{\left(k^2-q^2\right)^2} \\ \text{Anti}-\text{symmetric}: \frac{\tan qh}{\tan ph} &= -\frac{\left(k^2-q^2\right)^2}{4k^2qp} \\ p^2 = -\frac{\omega^2}{c_L^2} - k^2,\ q^2 &= -\frac{\omega^2}{c_T^2} - k^2, \text{ and } k = \frac{\omega}{v_p} \end{aligned} \tag{4}$$

where h, k, c_L, c_T, v_p and ω are the plate thickness, wave-number, velocities of longitudinal and transverse modes, phase velocity and wave circular frequency, respectively.

The equation is solved iteratively to estimate the wave propagation speed at any given frequency-thickness ratio, and, as expected, this equation implies that Lamb waves are dispersive regardless of propagation mode; resulting in a propagation speed that depends on the frequency that must then accounted for in the ray tracing method.

As the problem is formulated by assuming an infinite plate, by definition, Lamb waves have no particle motion in the y-direction. Motion in the y-direction in plates is found in the so-called Sh or shear-horizontal wave modes. These have no motion in the x- or z-directions, and are thus complementary to the two Lamb wave modes. Although this wave mode is not generally used for SHM applications, in the case of isotropic plates, the velocity of the first order shear propagation mode $Sh0$ has been mathematically proven to be equal to the anti-symmetric (bending) propagation mode $A0$[45].

Wave speed and dispersion in composite materials

Composite materials present characteristic anisotropic stiffness properties that have a significant influence on the propagation speed and media dispersion for elastic waves[46]. The stiffness transfer matrix method (STMM) has proven to be a good approximation in order to estimate the wave propagation speed[47], this methodology is well suited for multilayered media as it condenses the system into four equations, eliminating all other intermediate interfaces. It can be calculated for each media before the tracing of the ray propagation map and the propagation speed of each individual ray can be later interpolated from it based on its travelling direction angle and wave mode.

Assuming all composite layers behave as orthotropic media and following Hooke's law generalized for a two-dimensional shell, the layer stiffness matrix expressed in the laminate coordinates (rotated around the laminate perpendicular axis) C defines the relation between layer strains and stresses as:

$$\begin{Bmatrix} \sigma_{11} \\ \sigma_{22} \\ \sigma_{33} \\ \sigma_{23} \\ \sigma_{13} \\ \sigma_{12} \end{Bmatrix} = \begin{pmatrix} C_{11} & C_{12} & C_{13} & 0 & 0 & C_{16} \\ C_{12} & C_{22} & C_{23} & 0 & 0 & C_{26} \\ C_{13} & C_{23} & C_{13} & 0 & 0 & C_{36} \\ 0 & 0 & 0 & C_{44} & C_{45} & 0 \\ 0 & 0 & 0 & C_{45} & C_{55} & 0 \\ C_{16} & C_{26} & C_{36} & 0 & 0 & C_{66} \end{pmatrix} \begin{Bmatrix} \varepsilon_1 \\ \varepsilon_2 \\ \varepsilon_3 \\ \gamma_{23} \\ \gamma_{13} \\ \gamma_{12} \end{Bmatrix} \tag{5}$$

where σ_{ij} represent the material stress and ε_i and γ_{ij} represent the strain and shear angles respectively.

Applying Newtons second law to the stiffness matrix from Equation 5 and considering the small linear strain displacement approximation, given by:

$$\varepsilon_{i,j} = \frac{1}{2}\left(\frac{\partial u_j}{\partial x_i} + \frac{\partial u_i}{\partial x_j}\right) \tag{6}$$

the internal forces can be converted into internal stresses, resulting in $\nabla\dot{\sigma} = \rho\ddot{u}$. It is possible to then solve the resulting linear system of equations by imposing a sinusoidal wave solution in displacements of the form:

$$(u_1, u_2, u_3) = (U_1, U_2, U_3)e^{ik(x_1+\alpha x_3 - v_p t)} \tag{7}$$

where U_1, U_2, and U_3 are the amplitudes of the harmonic motions in time and space and v_p is the phase velocity of the wave.

Therefore, the equations of motion can be rewritten in matrix form as:

$$\begin{pmatrix} C_{11}-\rho v_p^2+C_{55}\alpha^2 & C_{16}+C_{45}\alpha^2 & (C_{13}+C_{55})\alpha \\ C_{16}+C_{45}\alpha^2 & C_{66}-\rho v_p^2+C_{44}\alpha^2 & (C_{36}+C_{45})\alpha \\ (C_{13}+C_{55})\alpha & (C_{36}+C_{45})\alpha & C_{55}-\rho v_p^2+C_{33}\alpha^2 \end{pmatrix} \begin{Bmatrix} U_1 \\ U_2 \\ U_3 \end{Bmatrix} = 0 \tag{8}$$

The system from Equation 8 can only present a non-trivial solution when its determinant equals zero; therefore, it could be studied as an eigenvalue problem to obtain the values of α, resulting in a six-order equation with only even coefficients[45,47].

Once solved, the values of α are found to be related in pairs:

$$\alpha_1 = -\alpha_2, \quad \alpha_3 = -\alpha_4, \quad \alpha_5 = -\alpha_6 \tag{9}$$

It is then possible to rewrite the expressions for displacements and layer stresses as a function of α_j, as follows:

$$(u_1, u_2, u_3) = \sum_{j=1}^{6} (1, V_j, W_j)\, U_1 e^{ik(x_i + \alpha_j x_3 - v_p t)} \tag{10}$$

$$(\sigma_{33}, \sigma_{13}, \sigma_{23}) = \sum_{j=1}^{6} (D_{1j}, D_{2j}, D_{3j})\, U_1 e^{ik(x_i + \alpha_j x_3 - v_p t)} \tag{11}$$

Values for the matrix terms V_j, W_j, D_{ij}, and α_j can be found in[47]; they are not written here due to space constraints. Defining a stress displacement vector $\mathbf{s}(x_3) = (u_1, u_2, u_3, \sigma_{33}, \sigma_{13}, \sigma_{23})$, the relation for wave propagation in each each layer is:

$$\begin{pmatrix} 1 & 1 & 1 & 1 & 1 & 1 \\ V_1 & V_2 & V_3 & V_4 & V_5 & V_6 \\ W_1 & W_2 & W_3 & W_4 & W_5 & W_6 \\ D_{11} & D_{12} & D_{13} & D_{14} & D_{15} & D_{16} \\ D_{21} & D_{22} & D_{23} & D_{24} & D_{25} & D_{26} \\ D_{31} & D_{32} & D_{33} & D_{34} & D_{35} & D_{36} \end{pmatrix} \begin{Bmatrix} U_{11} e^{k\alpha_1 x_3} \\ U_{12} e^{k\alpha_2 x_3} \\ U_{13} e^{k\alpha_3 x_3} \\ U_{14} e^{k\alpha_4 x_3} \\ U_{15} e^{k\alpha_5 x_3} \\ U_{16} e^{k\alpha_6 x_3} \end{Bmatrix} e^{ik(x_1 - v_p t)} = \begin{Bmatrix} u_1 \\ u_2 \\ u_3 \\ \sigma_{33} \\ \sigma_{13} \\ \sigma_{23} \end{Bmatrix} \tag{12}$$

Guaranteeing continuity by solving Equation 12 at the top and bottom of each layer, it is possible to obtain a relation between the upper and lower surfaces of the plate. Therefore, for a laminate of n layers, the expression would be:

$$\{s_t\} = [T^n][T^{n-1}]...[T^1]\{s_b\} = \prod_{j=1}^{n} [T^j]\{s_b\} = [A]\{s_b\} \tag{13}$$

$$\begin{Bmatrix} \{u_t\} \\ \{\sigma_t\} \end{Bmatrix} = \begin{pmatrix} [A_{uu}] & [A_{u\sigma}] \\ [A_{u\sigma}] & [A_{\sigma\sigma}] \end{pmatrix} \begin{Bmatrix} \{u_b\} \\ \{\sigma_b\} \end{Bmatrix} \tag{14}$$

Stress-free boundary conditions are then guaranteed in the top and bottom layers as $\{s_t\} = \{s_b\} = 0$; hence, the dispersion curves in terms of the phase velocity v_p can be computed as the solution of the determinant $|A_{u\sigma}| = 0$.

While the phase velocity, v_p, determines the speed at which each of the frequency components of the wave travel through a medium, the group velocity, defined as $v_g = \frac{dv_p}{dk}$, refers to the velocity at which the envelope of the wave packet propagate. In simpler terms, it is the speed at which the shape or modulation of a wave moves through space. The group velocity takes into account the entire waveform or wave packet, which may consist of a combination of different frequencies.

In a dispersive medium, where different frequencies of a wave travel at different speeds, the group velocity v_g must be different from the phase velocity v_p and the dispersion relation can be obtained via these two values. In order to trace the ray map for a defined time point the rays are then propagated at the phase velocity corresponding to the central frequency of the wave packet (maximum of the Fourier transform of the signal) this is an approximation, as the signal will be later recovered at the sensors taking into account the complete dispersion curve.

The shear wave propagation mode ($Sh0$) could also be obtained via this method but it is not accounted for in the model, as its usefulness for SHM applications is negligible compared with the other modes and only the $S0$ and $A0$ modes are considered and each is modeled with independent rays.

Ray signal recovery

In the case of active interrogation a tone burst is typically used as an excitation signal, usually consisting of a 10 V to 50 V peak to peak sine wave modulated by a Hamming window. These signals are named with the convention BURSTn where n represents the width of the window in number of periods, and in the case of aeronautic lightweight structures, the frequency of these signals is typically studied in the range of 100 kHz to 500 kHz.

The signal information is carried independently on each ray in the frequency domain, via a sufficiently large amount of terms of their Fourier transform, and could then be altered as the ray propagates through the model due to different effects, such as material damping which is considered as a factor over the signal amplitude A, following an exponential law:

$$A = A_0 \mathrm{e}^{-\omega \xi t} \tag{15}$$

where ξ is the material damping coefficient.

The signal is then recovered at each point applying the time shift property of the Fourier transform:

$$x(t - t_0) \longleftrightarrow e^{-i\omega t_0} X(\omega) \tag{16}$$

as the signal is dispersive, the phase velocity as a function of frequency $v_p(\omega)$, estimated in the previous section, is accounted for as follows:

$$x(t - t_0) \longleftrightarrow \sum_{j=0}^{N} e^{-i\omega_j \frac{d}{v_p(\omega_j)}} X_j(\omega_j) \tag{17}$$

where d is the distance along the ray path where the signal is to be obtained.

The method has been developed focusing on the characteristics of a piezoelectric transducer. As explained previously, due to the sensors low weight and their ability of both generating and measuring guided elastic waves they are ideal for SHM systems. Signals obtained unavoidably contain multiple modes requiring complex signal processing techniques to extract useful information. Moreover, PZT sensors may also reveal certain nonlinear behavior and hysteresis under large strains/voltages or at high temperature. Brittleness, low fatigue life, etc., may be some other concerns limiting application[48].

To include the PZT sensors in the simulation, they are modeled as a circle boundary. This boundary does not interact with the incident rays, however the intersection time points (t_i and t_e) are captured and the ray signal is integrated between the line crossing the sensor area ($s_e - s_i$), as shown in Figure 1. This way allows the sensor to act as an integrator of the material strain over the area it covers[49,50], and the solution is obtained by superimposing the integrated signal of all the incident rays.

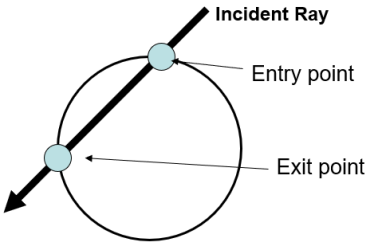

Figure 1. Schema of the PZT sensors model for the ray tracing algorithm

There are a number of significant advantages that arise from using this methodology, the main one is being able to avoid the need to calculate eigenrays to the sensors, therefore saving significant computation time, and being able to obtain a solution with the first iteration of the ray map.

As the sensors acts as a signal integrator, the dispersive effect on the signal is inherently captured by modelling its area. This effect is significantly more relevant for cases where the signal wavelength is comparable to the sensor dimensions, and may have some noticeable effect in the signal measured.

On the contrary, a larger number of initial rays is needed to achieve a good solution, and later reflections may be captured imprecisely or not be captured at all due to the low number of rays that may cross the sensor, although this could be solved by iteratively increasing the number of rays until achieving a converged solution.

Method application - results and discussion

This section presents two case studies in order to validate the methodology and demonstrate its applicability:

- Isotropic metallic plate, for a basic methodology validation and boundary coefficients adjustment.
- Composite UAV wing lower cover demonstrator, to test the methodology on a more real structure example. This is performed in two phases: first with artificial damages, via added masses to the structure and second with a real BVID resulting from a 7 J impact.

Isotropic metallic plate analysis and validation

The methodology is first validated against a physical test in a rectangular aeronautic grade 2023-T3 aluminium plate. The test is instrumented with an array of 7, evenly distributed, 12 mm piezoelectric (PZT ceramic) sensors, and the data is recorded with an Acellent SCAN GENIE system, with a sampling frequency of 48 MHz. The plate is simply supported on two of its sides. The effect of the support is considered negligible and for the simulation and it was opted to just assume a constant uniform energy loss in all of the boundary; weight of cabling and instrumentation are also not considered in the simulation.

The results of a ray tracing simulation, for 801 initial rays, are shown as a heat-map in Figure 2 a) at a time $t = 8 \times 10^{-6}$ s, when emitting a 300 kHz BURST3 signal from transducer $PZT1$. Numbering and position of the piezoelectric sensors is also shown in the figure.

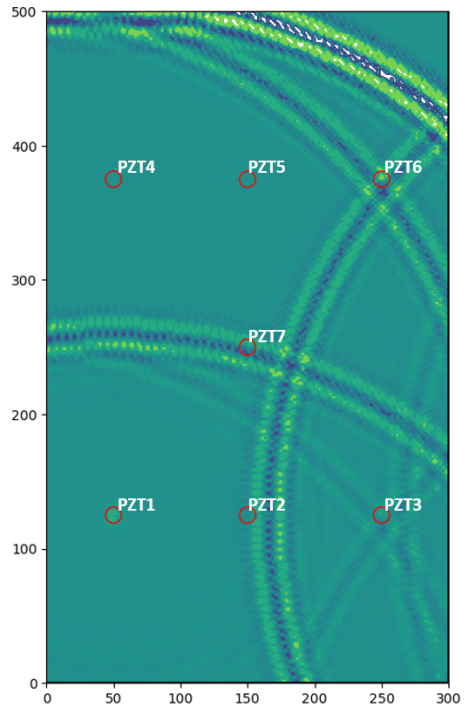

(a) Ray signal heat-map.

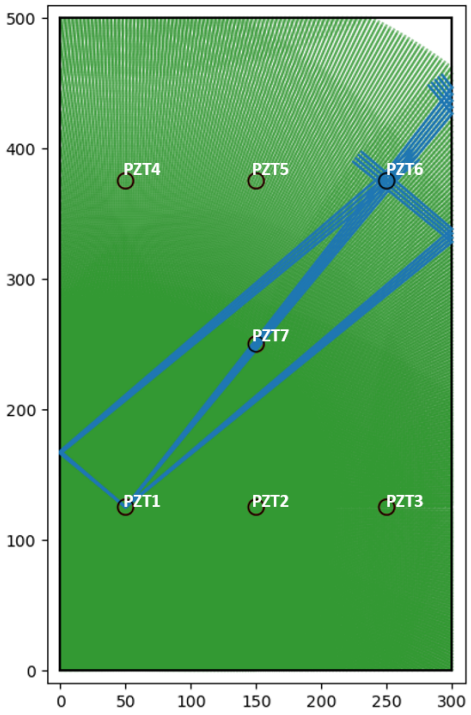

(b) Rays intersecting sensor $PZT6$ originating from sensor $PZT1$.

Figure 2. Ray tracing model results at $t = 8 \times 10^{-6}$ s.

The heat-map shown in Figure 2 a) is calculated by mapping the rays signal over a square grid with a characteristic length of 2 mm. The figure shows how the elastic waves propagate through the plate and interact with each boundary and how the energy is being dissipated after each reflection.

In order to capture the results on a selected transducer, the rays that intersect the sensor must be detected and integrated over its length. As an example, all rays captured by transducer $PZT6$ when emitting a signal from $PZT1$ at $t = 8 \times 10^{-6}$ s are shown graphically in Figure 2 b).

The signal carried by each ray is then integrated numerically over the length travelled by each ray though the sensor and added together. The results are shown in Figure 3, compared with the experimental data.

An analytic signal is defined in terms of a real part and an imaginary part; its magnitude is related to the magnitude spectrum, and its phase angle its phase spectrum. Features, such as standard deviation of amplitude, standard deviation of phase, and signal energy can be extracted from these spectrums.

The real and imaginary parts of the analytic signal are related by the Hilbert transform; which takes a function $u(t)$ of a real variable and produces another function of a real variable $H(u)(t)$. The Hilbert transform can therefore be thought of as the convolution of $u(t)$ with the Cauchy kernel, $h(t) = \frac{1}{\pi t}$, and it is written explicitly as:

$$H(u)(t) = \frac{2}{\pi} \lim_{\varepsilon \to 0} \int_{\infty}^{\varepsilon} \frac{u(t-\tau) - u(t+\tau)}{2\tau} d\tau \qquad (18)$$

By taking the real function $u(t)$ as the signal measured in our system, we can apply this methodology to obtain additional information and aid with the visual representation of the data. The Hilbert transform has been historically widely used for signal processing in many disciplines, and particularly for SHM can be extremely useful to interpret the signal results[51].

The absolute value of the Hilbert transform gives a representation of the instantaneous amplitude of the function, as shown in Figure 3 where it is plotted alongside the sensors signal to aid with its visual interpretation.

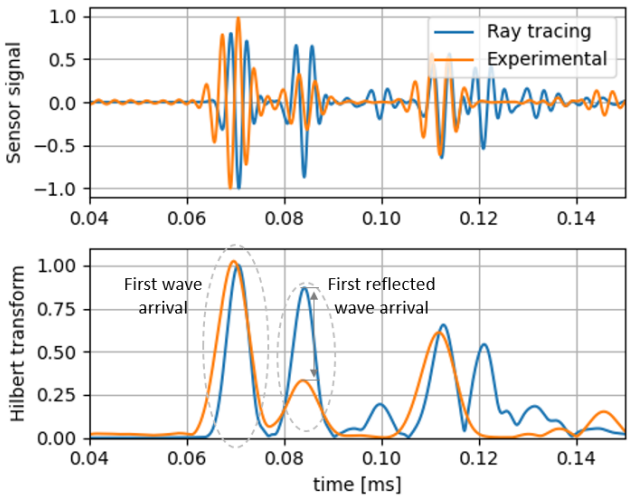

Figure 3. Result signal and Hilbert transform for path 1-6.

Shown in Figure 3, the intensity of the first peak of the received signal is related to the amplitude of the input signal and material properties (damping or dispersion) during the wave path. Its absolute value, however, is governed by many different factors such as piezo-electric characteristics of the sensors or the amplification factor of the acquisition system. These factors, although, out of the scope of this study are assumed to have a linear effect on the signal and therefore the experimental signal is normalized when compared with the simulated data.

Second and successive peaks on the received signal are related to wave reflections on the plate edges (not taking into consideration the arrival of the A0 wave, that it is not relevant in the time frame studied due to its relatively low propagation speed in this condition). Their relative amplitude is therefore governed by the energy dissipated in those reflections. This is taken into account in the simulation by the boundary losses coefficient set at the edges ε_E.

A parametric study is performed evaluating the boundary losses coefficient ε_E in the interval of $[0, 0.9]$ and the normalized difference of the second peak amplitude is evaluated, with a fixed a mode conversion factor $f_{mc} = 0.9$. In this case all the remaining energy is reflected, therefore the energy transmission factor is not taken into account.

The normalized error on the second peak resulting of this study is shown in Figure 4, along with its average and standard deviation for each of the sensor paths present in the plate. The average of each measure is joined together to highlight the tendency of the data.

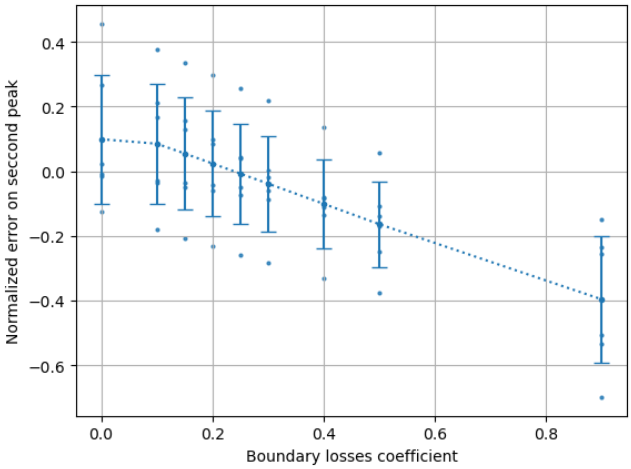

Figure 4. Aluminium plate error on second peak.

Figure 4 shows is a significant dispersion in the data; this dispersion has been mainly attributed to factors not accounted for in the simulation, such as precission in sensor position and adhesion to the plate, plate material imperfections, sensors and cabling weight, and differences in the edges and supports of the plate which are only represented in the simulation as the uniform factor ε_E. However, there is still a clear linear tendency that shows an optimum zero average at a value $\varepsilon_E = 0.25$.

Therefore, based on the results of this study the boundary losses factor ε_E is fixed at 0.25, as it gives the best match with the experimental results considering the methodology limitations described.

The results obtained for a number of relevant paths are shown in Figure 5 compared with the experimental test results, for a simulation with 801 initial rays and assuming the boundary losses factor $\varepsilon_E = 0.25$ uniform and applied in all four boundaries of the plate.

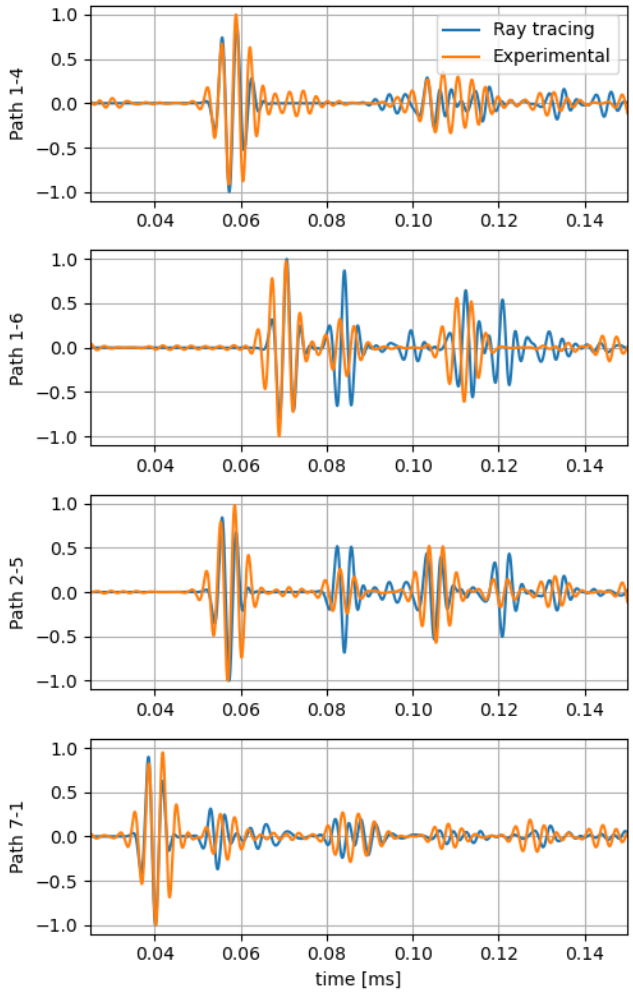

Figure 5. Normalized signal intensity comparison for relevant sensor paths.

As shown Figure 5 in the simulation presents a very good agreement with the experimental data after the fitting for all configurations explored. Initial wave packet and reflections appear with precision both in arrival times and amplitude in the simulation results, although some differences can be observed on some of the later reflections that may be explained due to signal error accumulation, sensor positioning and bonding imperfections, geometrical differences or imperfections in the boundaries, materials and sensors and cable and sensors weight.

The correlation presented by this method is comparable in accuracy to other simulation methodologies, such as finite elements or spectral element models, but the computation time is significantly shorter, in orders of magnitude for some cases[52], making this method especially attractive for generating large amount of data points that could be used in cases of artificial intelligence training databases.

Artificial damages on composite wing demonstrator

In order to evaluate the simulation behavior in the presence of damage, the methodology is compared against a physical demonstrator of the front left wing lower cover of the remotely piloted aircraft system LIBIS, designed and built by the Technical University of Madrid.

The specimen is instrumented with an array of 8, 12 mm piezoelectric (PZT) sensors, shown in Figure 6, and the data is again recorded with the same Acellent SCANGENIE system, using a sampling frequency of 48 MHz.

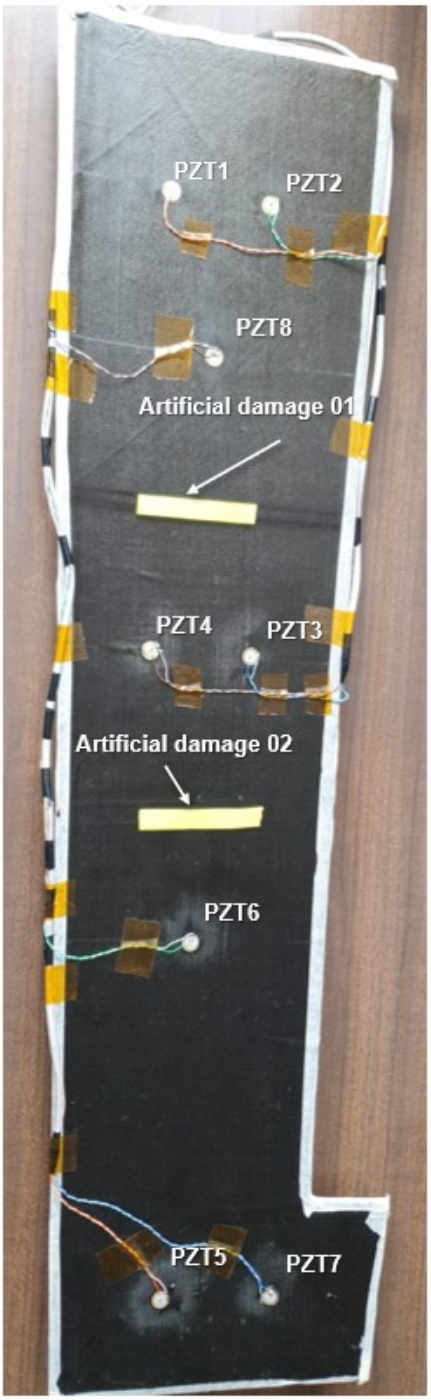

Figure 6. Example test configurations evaluated on LIBIS wing prototype. Transducers and artificial damages location and numbering.

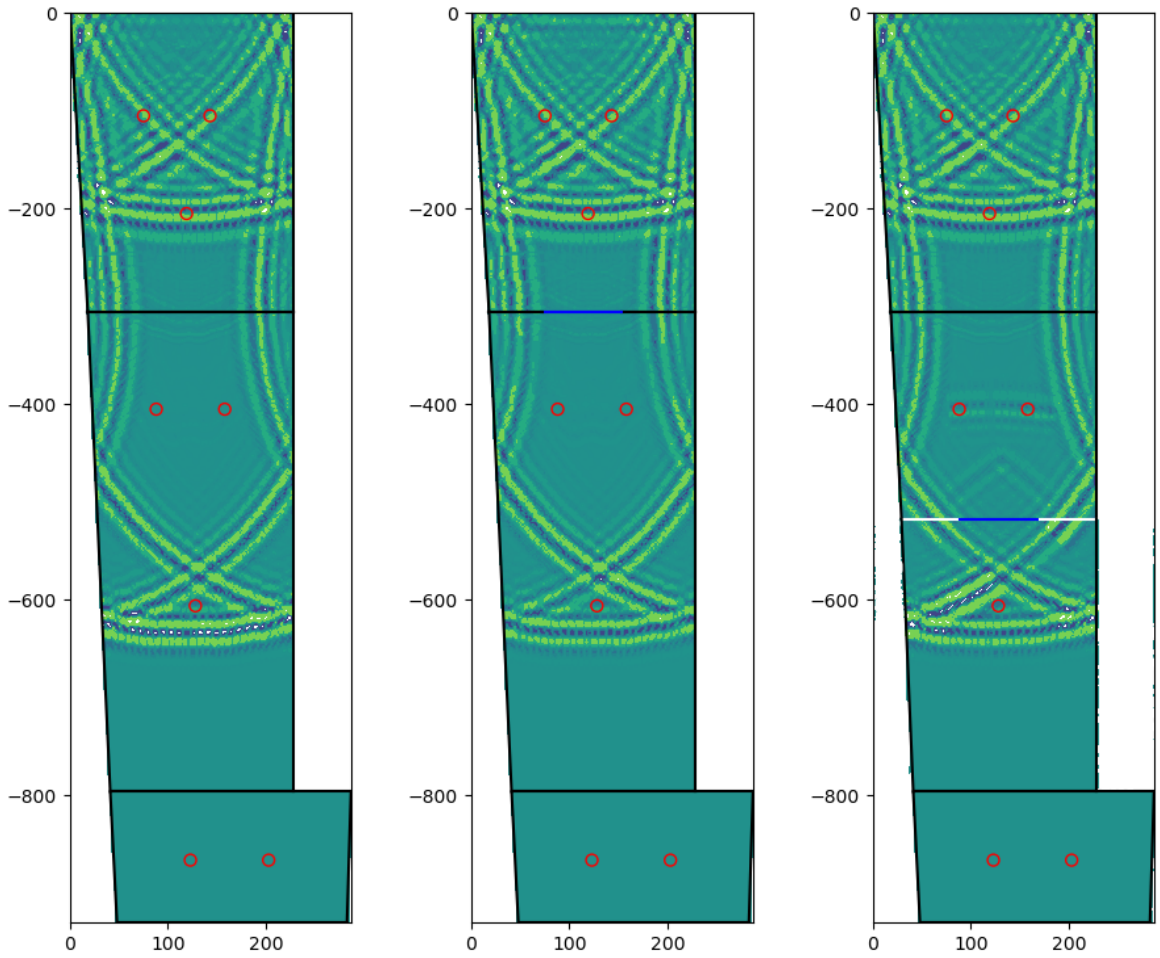

(a) Intact configuration. (b) Artificial damage 01. (c) Artificial damage 02.

Figure 7. Results contours for the configurations evaluated on LIBIS wing prototype, at $t = 0.5\,\mathrm{ms}$. Origin: $PZT8$.

Artificial damages to emulate the effect of a possible delamination have been introduced in the specimen, as shown in Figure 6. These damages are introduced as added masses in order to alter the dynamic behavior of the structure. Three sets of tests were performed considering the intact structure, the structure with the artificial damage 01 and the structure with artificial damage 02. The input signal used consist on a BURST3 at $350\,\mathrm{kHz}$ at $40\,\mathrm{V}$; test results are presented as an average of 3 runs.

A contour plot of the simulation results for each case is shown in Figure 7. The simulation is run with 1201 initial rays originating from piezo-electric transducer $PZT8$, artificial damage areas are simulated as linear boundary segments. Intact plate simulation results are shown in Figure 7 a) and Figure 7 b) and c) show the results for artificial damages 01 and 02 respectively.

In order to quantify the effect of the damage on the system, both the energy reflected and dissipated in the artificial boundary were adjusted manually based on the shortest linear propagation path, in this case corresponding to between sensors $PZT3$ and $PZT6$, described in [52].

The raw signal obtained with the tests is compared against the simulation in Figure 8 for the path between$PZT8$ and $PZT6$, both centered in the plate and each located at opposite sides of both artificial damage 01 and 02.

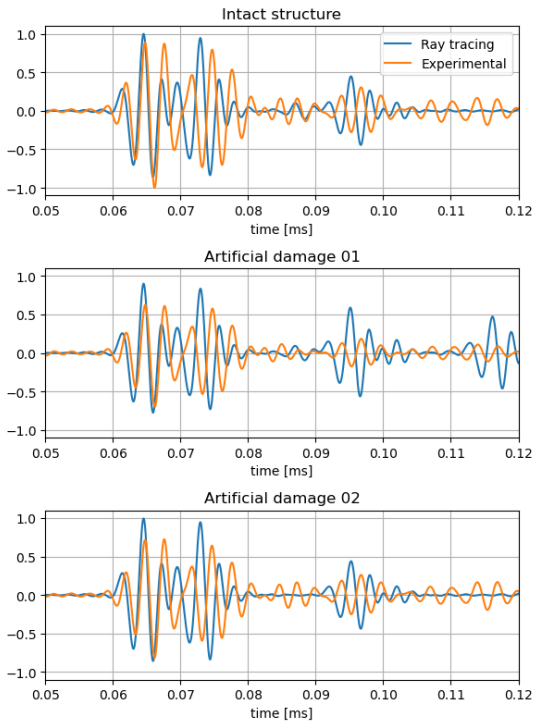

Figure 8. Simulation vs. Test results raw signal comparison with artificial damages for path 8-6.

Although in this case there are much higher uncertainties in the experiment and the differences are more significant than the metallic plate case, the model predictions is still consistent with the experimental data when estimating the effect of the artificial damages on the signal and its effect can be observed and quantified with the sensor network data.

Real impact damage study on composite wing demonstrator

To evaluate the effect of a real damage on The LIBIS panel is then subjected to a 7 J impact, with a 1 kg steel spherical impactor, using a 70 cm tall drop tower. The impact is located in the center of the panel in a similar location as the artificial damage 01, at approximately 6 cm from the lower cover trailing edge. The impact is performed on the outer face in order to emulate a possible real BVID due to some external in-service damage.

Images of the resulting impact are shown in Figure 9. As expected, the effects of the damage can be more clearly observed on the opposite side of the impact, appearing as some fiber breakage, shown in Figure 9 b), while on the impact side (Figure 9 a)) they appear only as a small indentation.

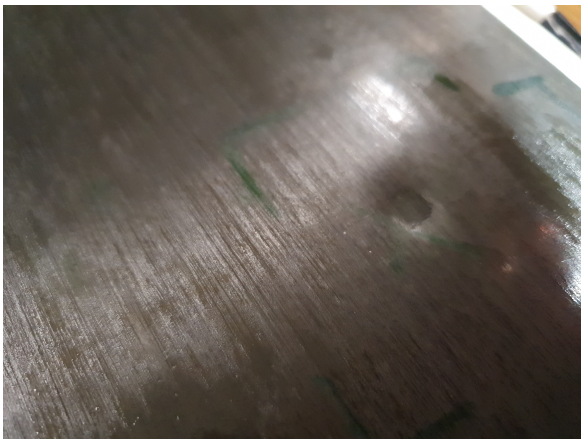

(a) Impact side

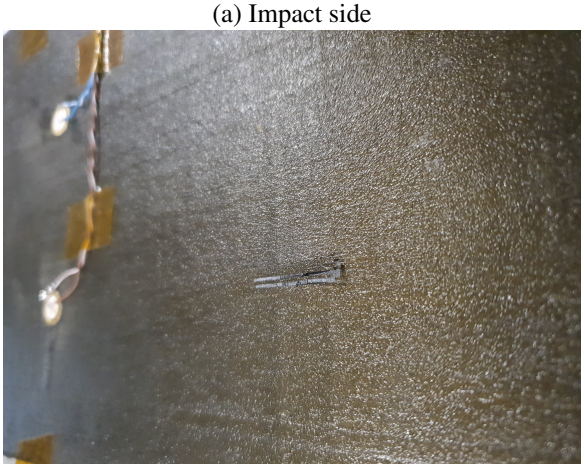

(b) Opposite impact side

Figure 9. 7 J impact damage pictures

To fully characterize the impact, the damaged area is inspected with an Olympus OmniScan MX2 and its results of the A, B and C-scan are shown in Figure 10, where significant delaminations and fiber and matrix crackings spanning an approximate area of 23 cm^2 and and extension of the damage through the complete plate thickness can be observed.

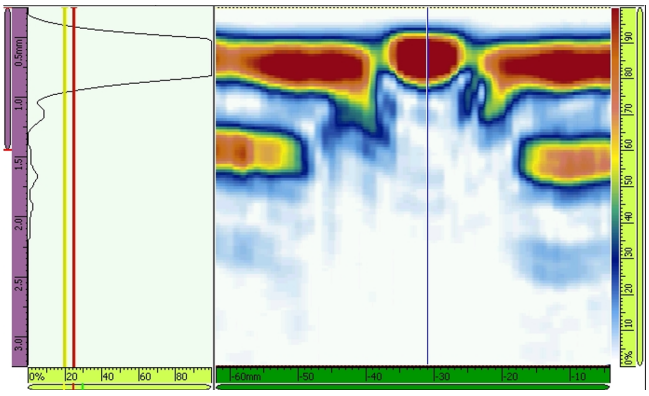

(a) A and B-Scan

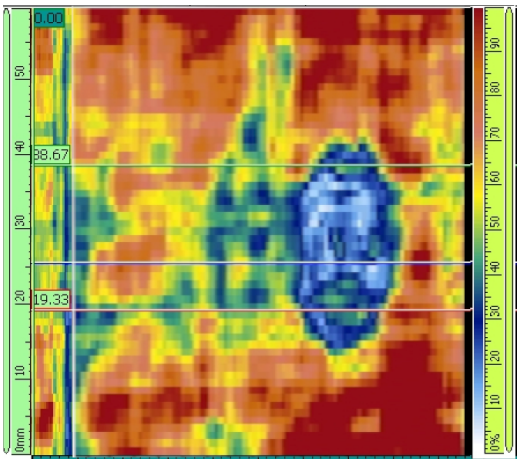

(b) C-Scan

Figure 10. NDT results on damage location

This damaged area is then introduced in the simulation, assuming a uniform boundary reflection factor $f_{tr} = 0.1$ and dissipation factor of $\varepsilon_E = 0.5$.

Instant amplitude difference results of relevant sensor path $PZT8 - PZT6$, located at both sides of the damaged area are shown in Figure 11. Damage energy dissipation characteristics has been adjusted manually in the simulation in order to match the experiment results.

As the damage is not directly located across the line joining sensors $PZT8$ and $PZT6$ its effect is clearly visible in the second wave packet arrival, while the first wave packet remains unchanged from the intact configuration. Its also pretty obvious from the figures that this damage effect in the signals is significantly more noticeable than the simulated damages shown in the previous section.

Again, main differences can be explained with the same reasoning exposed in the previous sections, but additionally this case presents the complications inherent to the damage characterization. A small but appreciable frequency shift is also observed in the experimental results, which does not appear in the ray tracing simulation as the damage is still modelled as a zero width boundary.

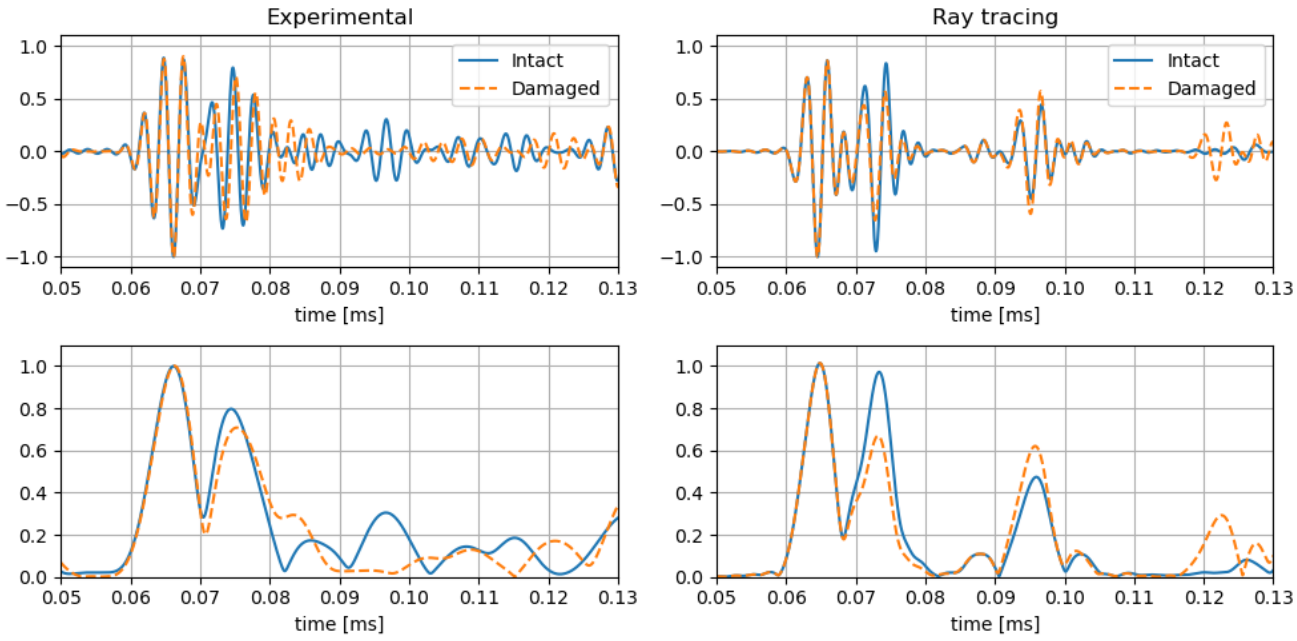

Figure 11. Results contours for the configurations evaluated on LIBIS wing prototype, at $t = 0.5\,\mathrm{ms}$. Origin: $PZT8$.

Conclusions

The conducted tests on the metallic plate have proven instrumental in validating the proposed ray tracing methodology in a representative structure; the method demonstrates its capability to predict the guided Lamb waves propagation accurately and as shown in the results, both, initial wave packet and reflections appear with precision in arrival times and amplitude. This demonstrates and enhances the practical applicability of the methodology, and therefore it increases the confidence when applying the validated ray tracing method to more complex composite structures.

The boundaries dissipation factors optimization has converged to a reasonable low value and is consistent with the expected magnitude for these kind of structures. This value is then used for the tests on the CFRP LIBIS wing lower cover demonstrator.

Results on the CFRP LIBIS wing lower cover show a significant match and similar tendencies in the presence of damage between the tests and numerical analysis. The possibility of damage could be identified, and its location and extent could be assessed by analyzing the data with cross correlation algorithms or the information could be used to feed an artificial intelligence model.

The correlation can be improved with a better characterization of the boundaries considering also the effects on frequency and propagation mode. This effect accumulates on each reflection and the differences increase with the time of study. Exact sensor positioning, manufacturing imperfections and other factors, discussed previously, can also alter the results and its influence is also accumulated in time.

The results of real damage are difficult to interpret due to all the uncertainties present in this analysis, however, the methodology proposed can still present a good degree of accuracy and some of the effects on the signal are still captured and can be observed in the presented results. Further study should be performed to improve the simulation results, that could include a characterization of damage dispersive characteristics by simulating a realistic damage area in the model.

Declaration of conflicting interests

The author(s) declared no potential conflicts of interest with respect to the research, authorship, and/or publication of this article.

Funding

This project has received funding from the national research program Retos de la Sociedad under the Project STARGATE: Desarrollo de un sistema de monitorización estructural basado en un microinterrogador y redes neuronales (reference PID2019-105293RB-C21).

References

1. Tuo H, Lu Z, Ma X et al. Damage and failure mechanism of thin composite laminates under low-velocity impact and compression-after-impact loading conditions. *Composites Part B* 2019; 163: 642–654. DOI:10.1016/j.compositesb.2019.01.006.
2. Li X, Ma D, Liu H et al. Assessment of failure criteria and damage evolution methods for composite laminates under low-velocity impact. *Composite structures* 2019; 207: 727–739. DOI:10.1016/j.compstruct.2018.09.093.
3. Wang J, Wang H, Chen B et al. A failure mechanism based model for numerical modeling the compression-after-impact of foam-core sandwich panels. *Composites Science and Technology* 2017; 151: 258–67. DOI:10.1016/j.compscitech.2017.08.027.
4. Guinard S, Allix O, Guedra-Degeorges D et al. A 3d damage analysis of low velocity impacts on laminated composites. *Composites Science and Technology* 2002; 62: 585–9. DOI:10.1016/S0266-3538(01)00153-1.

5. on Structural Health AISC. *Guidelines for Implementation of Structural Health Monitoring on Fixed Wing Aircraft*, 2021. DOI:https://doi.org/10.4271/ARP6461A. URL https://doi.org/10.4271/ARP6461A.
6. Barthorpe RJ. *On model-and data-based approaches to structural health monitoring*. PhD Thesis, University of Sheffield, 2010.
7. Seno AH, Khodaei ZS and Aliabadi MF. Passive sensing method for impact localisation in composite plates under simulated environmental and operational conditions. *Mechanical Systems and Signal Processing* 2019; 129: 20–36. DOI:10.1016/j.ymssp.2019.04.023.
8. Wu S, Zhang Z, Chen J et al. Characterisation of stress corrosion durability and time-dependent performance of cable bolts in underground mine environments. *Engineering Failure Analysis* 2023; 150: 107292. DOI: https://doi.org/10.1016/j.engfailanal.2023.107292. URL https://www.sciencedirect.com/science/article/pii/S1350630723002467.
9. García Alonso J. *Monitorización de estructuras aeronáuticas mediante técnicas de inteligencia artificial*. PhD Thesis, Technical University of Madrid, 2016.
10. Ostachowicz W, Kudela P, Malinowski P et al. Damage localisation in plate-like structures based on pzt sensors. *Mechanical Systems and Signal Processing* 2009; 23: 1805–1829. DOI:10.1016/j.ymssp.2008.10.011.
11. Qing X, Li W, Wang YS et al. Piezoelectric transducer-based structural health monitoring for aircraft applications. *Sensors* 2019; 19: 545. DOI:10.3390/s19030545.
12. Farrar CR and Worden K. An introduction to structural health monitoring. *Philosophical Transactions of the Royal Society A: Mathematical, Physical and Engineering Science* 2006; 365. DOI:10.1098/rsta.2006.1928.
13. Charles H Keilers J and Chang FK. Identifying delamination in composite beams using built-in piezoelectrics: Part i – experiments and analysis. *Journal of Intelligent Material Systems and Structures* 1995; 6(5): 649–663. DOI:10.1177/1045389X9500600506.
14. Lin M, Qing X, Kumar A et al. Smart layer and smart suitcase for structural health monitoring applications. In *SPIE Smart Structures and Materials + Nondestructive Evaluation and Health Monitoring*, volume 4332. p. 98–106. DOI:10.1117/12.429646.
15. Zhao X, Gao H, Zhang G et al. Active health monitoring of an aircraft wing with embedded piezoelectric sensor/actuator network: I. defect detection, localization, and growth monitoring. *Smart Materials and Structures* 2007; 16: 1208–1217. DOI:10.1088/0964-1726/16/4/032.
16. López AF. *Detección de daño en estructuras aeronáuticas mediante sensores piezoeléctricos y de fibra óptica*. PhD Thesis, Technical University of Madrid, 2009.
17. Aloisio A, Di Battista L, Alaggio R et al. Sensitivity analysis of subspace-based damage indicators under changes in ambient excitation covariance, severity and location of damage. *Engineering Structures* 2020; 208: 110235. DOI:https://doi.org/10.1016/j.engstruct.2020.110235. URL https://www.sciencedirect.com/science/article/pii/S0141029619328676.
18. Mendler A, Döhler M and Ventura CE. A reliability-based approach to determine the minimum detectable damage for statistical damage detection. *Mechanical Systems and Signal Processing* 2021; 154: 107561. DOI:https://doi.org/10.1016/j.ymssp.2020.107561. URL https://www.sciencedirect.com/science/article/pii/S088832702030947X.
19. de Luca A, Perfetto D, de Fenza A et al. A sensitivity analysis on the damage detection capability of a lamb waves based shm system for a composite winglet. In *Proceeding of the AIAS 2018 International Conference on Stress Analysis*, volume 12. Procedia Structural Integrity, pp. 578–588.
20. Cross EJ, Gibson SJ, Jones MR et al. *Physics-Informed Machine Learning for Structural Health Monitoring*. Springer International Publishing. ISBN 9783030817169, 2021. p. 347–367. DOI:10.1007/978-3-030-81716-9_17. URL http://dx.doi.org/10.1007/978-3-030-81716-9_17.
21. Kudela P, Radzienski M and Ostachowicz W. Impact induced damage assessment by means of lamb wave image processing. *Mechanical Systems and Signal Processing* 2018; : 23–36DOI: 10.1016/j.ymssp.2017.09.020.
22. Kudela P, Radzienski M and Ostachowicz W. Wave propagation modeling in composites reinforced by randomly oriented fibers. *Journal of Sound and Vibration* 2018; 414: 110–125. DOI:10.1016/j.jsv.2017.11.015.
23. Li F, Zhao Y, Cao P et al. Mixing of ultrasonic lamb waves in thin plates with quadratic nonlinearity. *Ultrasonics* 2018; 87: 33–43. DOI:10.1016/j.ultras.2018.02.005.
24. Ong W, Rajic N, Chiu W et al. Adhesive material property evaluation for improved lamb wave simulation. *International Journal of Adhesion & Adhesives* 2016; 71: 28–38. DOI: 10.1016/j.ijadhadh.2016.08.008.
25. Sánchez Iglesias F and Fernández López A. Rayleigh damping parameters estimation using hammer impact tests. *Mechanical Systems and Signal Processing* 2020; 135: 106391. DOI: https://doi.org/10.1016/j.ymssp.2019.106391.
26. Svendsen BT, Øiseth O, Frøseth GT et al. A hybrid structural health monitoring approach for damage detection in steel bridges under simulated environmental conditions using numerical and experimental data. *Structural Health Monitoring* 2023; 22(1): 540–561. DOI:10.1177/14759217221098998. URL https://doi.org/10.1177/14759217221098998. https://doi.org/10.1177/14759217221098998.
27. Chiappa A, Iakovlev S, Marzani A et al. An analytical benchmark for a 2d problem of elastic wave propagation in a solid. *Engineering Structures* 2021; 229: 111655. DOI: https://doi.org/10.1016/j.engstruct.2020.111655.
28. Kim KB, Nah MK, Kim BK et al. The natural frequencies of aisi 316 stainless steel and analytical simulation of a lamb wave excited by a point source. *Wave Motion* 2022; : 103085DOI: https://doi.org/10.1016/j.wavemoti.2022.103085.
29. He XJ, Li JS, Huang XY et al. Solving elastic wave equations in 2d transversely isotropic media by a weighted runge-kutta discontinuous galerkin method. *Petroleum Science* 2022; DOI: https://doi.org/10.1016/j.petsci.2022.10.007.
30. Buckley T, Ghosh B and Pakrashi V. A feature extraction & selection benchmark for structural health monitoring. *Structural Health Monitoring* 2022; 0(0): 14759217221111141. DOI:10.1177/14759217221111141.
31. Nguyen A, Kodikara KTL, Chan TH et al. Deterioration assessment of buildings using an improved hybrid model updating approach and long-term health monitoring data.

Structural Health Monitoring 2019; 18(1): 5–19. DOI:10.1177/1475921718799984.

32. Aila T and Laine S. Understanding the efficiency of ray traversal on gpus. In *Proceedings of the Conference on High Performance Graphics 2009*. HPG '09, New York, NY, USA: Association for Computing Machinery. ISBN 9781605586038, p. 145–149. DOI:10.1145/1572769.1572792. URL https://doi.org/10.1145/1572769.1572792.
33. Peterson JR, Jernigan JG, Kahn SM et al. Simulation of astronomical images from optical survey telescopes using a comprehensive photon monte carlo approach. *The Astrophysical Journal Supplement Series* 2015; 218(1): 14. DOI:10.1088/0067-0049/218/1/14.
34. Spencer GH and Murty MVRK. General ray-tracing procedure†. *J Opt Soc Am* 1962; 52(6): 672–678. DOI:10.1364/JOSA.52.000672.
35. Officer CB. *Introduction to the Theory of Sound Transmission: with Application to the Ocean.* McGraw-Hill Book Company, Inc., 1958. ISBN 0070476128, 9780070476127.
36. Hovem J. *Marine Acoustics-The Physics of Sound in Marine Environments*. Peninsula Publishing, Los Altos Hills, CA, USA, 2010. ISBN 978-0932146656.
37. Piqueras J, Pérez-Grande I, Sanz-Andres A et al. Calculation of linear conductances for thermal lumped models by means of the cmf method. *Acta Astronautica* 2020; 173: 76–85. DOI:10.1016/j.actaastro.2020.04.004.
38. Huang L, Zeng L, Lin J et al. Baseline-free damage detection in composite plates using edge-reflected lamb waves. *Composite Structures* 2020; 247: 112423. DOI:https://doi.org/10.1016/j.compstruct.2020.112423.
39. Malyarenko EV and Hinders MK. Ultrasonic lamb wave diffraction tomography. *Ultrasonics* 2001; 39(4): 269–281. DOI:https://doi.org/10.1016/S0041-624X(01)00055-5.
40. Heinze C, Sinapius M and Wierach P. Lamb Wave Propagation in Complex Geometries - Model Reduction with Approximated Stiffeners. In Cam L, Vincent, Mevel et al. (eds.) *EWSHM - 7th European Workshop on Structural Health Monitoring*. Nantes, France: IFFSTTAR, Inria, Université de Nantes, p. 0. URL https://hal.inria.fr/hal-01021067.
41. Shivaprasad SB, Saini1 A, Purushothaman P et al. Elastic wave propagation in polycrystalline materials using ray tracing model. In *19th World Conference on Non-Destructive Testing (WCNDT 2016)*, volume 2016-07. Procedia Structural Integrity, p. 0. URL https://www.ndt.net/?id=19401.
42. Gunawan A and Hirose S. Reflection of obliquely incident guided waves by an edge of a plate. *MATERIALS TRANSACTIONS* 2007; 48(6): 1236–1243. DOI:10.2320/matertrans.I-MRA2007852.
43. Cho Y and Rose JL. A boundary element solution for a mode conversion study on the edge reflection of lamb waves. *The Journal of the Acoustical Society of America* 1996; 99(4): 2097–2109. DOI:10.1121/1.415396.
44. Mindlin RD. Influence of rotatory inertia and shear deformation on flexural motion of isotropic, elastic plates. *Journal of Applied Mechanics* 1951; 18: 31–38.
45. Conry MJ. Notes on wave propagation in anisotropic elastic solids, 2005. URL https://www.acronymchile.com/downloads/anisotropic_with_lamb_waves.pdf.
46. Ma Z, Chen J, Li B et al. Dispersion analysis of lamb waves in composite laminates based on reverberation-ray matrix method. *Composite Structures* 2016; 136: 419–429. DOI:https://doi.org/10.1016/j.compstruct.2015.10.036. URL https://www.sciencedirect.com/science/article/pii/S026382231500968X.
47. Kamal A, Gresil M and Giurgiutiu V. *Comparative Study of Several Methods for the Calculation of Ultrasonic Guided Waves in Composites*. 2013. DOI:10.2514/6.2013-1901. URL https://arc.aiaa.org/doi/abs/10.2514/6.2013-1901. https://arc.aiaa.org/doi/pdf/10.2514/6.2013-1901.
48. Schulz M, Pai P and Inman D. Health monitoring and active control of composite structures using piezoceramic patches. *Composites, Part B* 1999; 30: 713–725. DOI:10.1016/S1359-8368(99)00034-7.
49. Ayers JP, Greve DW and Oppenheim IJ. Energy scavenging for sensor applications using structural strains. In *Smart Structures and Materials*, volume 5057. SPIE, p. 0. DOI:10.1117/12.482377.
50. Erturk A and Inman D. *Piezoelectric Energy Harvesting*. 1 ed. John Wiley & Sons, Ltd., 2011. ISBN 9781119991359.
51. Pines D and Salvino L. Structural health monitoring using empirical mode decomposition and the hilbert phase. *Journal of Sound and Vibration* 2006; 294(1): 97–124. DOI:https://doi.org/10.1016/j.jsv.2005.10.024. URL https://www.sciencedirect.com/science/article/pii/S0022460X05007029.
52. Sánchez Iglesias F and Fernández López A. Evaluating structural details' influence on elastic wave propagation for composite structures via ray tracing. *Sensors* 2023; 23(16). DOI:10.3390/s23167220. URL https://www.mdpi.com/1424-8220/23/16/7220.